






## Article

# Optimization of Airborne Antenna Geometry for Ocean Surface Scatterometric Measurements

Alexey Nekrasov <sup>1,2,3,\*</sup> , Alena Khachaturian <sup>1</sup>, Evgeny Abramov <sup>1,2</sup>, Dmitry Popov <sup>4</sup> ,  
Oleg Markelov <sup>1</sup> , Viktor Obukhovets <sup>1,5</sup> , Vladimir Veremyev <sup>1</sup> and Mikhail Bogachev <sup>1</sup> 

<sup>1</sup> Department of Radio Engineering Systems and Scientific-Research Institute “Prognoz”, Saint Petersburg Electrotechnical University, Professora Popova 5, 197376 Saint Petersburg, Russia; khachaturyan.al@gmail.com (A.K.); abramoves@gmail.com (E.A.); olegmarkelov@gmail.com (O.M.); vaomailru@mail.ru (V.O.); ver\_vi@mail.ru (V.V.); roges@yandex.com (M.B.)

<sup>2</sup> Institute for Computer Technologies and Information Security, Southern Federal University, Chekhova 2, 347922 Taganrog, Russia

<sup>3</sup> Institute of High Frequency Technology, Hamburg University of Technology, Denickestraße 22, 21073 Hamburg, Germany

<sup>4</sup> Sochi State University, Sovetskaya 26a, 354000 Sochi, Russia; damitry@mail.ru

<sup>5</sup> Institute for Radio Engineering Systems and Control, Southern Federal University, Engelsa 1, 347922 Taganrog, Russia

\* Correspondence: alexei-nekrassov@mail.ru; Tel.: +7-8634-360-484

Received: 26 July 2018; Accepted: 18 September 2018; Published: 20 September 2018



**Abstract:** We consider different antenna configurations, ranging from simple X-configuration to multi-beam star geometries, for airborne scatterometric measurements of the wind vector near the ocean surface. For all geometries, track-stabilized antenna configurations, as well as horizontal transmitter and receiver polarizations, are considered. The wind vector retrieval algorithm is generalized here for an arbitrary star geometry antenna configuration and tested using the Ku-Band geophysical model function. Using Monte Carlo simulations for the fixed total measurement time, we show explicitly that the relative wind speed estimation accuracy barely depends on the chosen antenna geometry, while the maximum wind direction retrieval error reduces moderately with increasing angular resolution, although at the cost of increased retrieval algorithm computational complexity, thus, limiting online analysis options with onboard equipment. Remarkably, the simplest X-configuration, while the simplest in terms of hardware implementation and computational time, appears an outlier, yielding considerably higher maximum retrieval errors when compared to all other configurations. We believe that our results are useful for the optimization of both hardware and software design for modern airborne scatterometric measurement systems based on tunable antenna arrays especially, those requiring online data processing.

**Keywords:** airborne scatterometer; multi-beam antenna configuration; star geometry; ocean surface; wind vector; retrieval accuracy

## 1. Introduction

Despite the recent decades’ great success of satellite radar observation technologies, airborne radars provide a powerful alternative for high-resolution measurements of the ocean surface. They are especially useful within local areas near complex-shaped coastlines, straights, and archipelagoes that largely perturb the surrounding flows and winds, leading to the formation of complex local currents and/or near-surface wind fields structures, and largely limiting the efficacy of sparse-grid satellite measurements. Depending on the measurement techniques used, particular components can be extracted, e.g., the over-surface wind fields can be retrieved by scatterometric measurements that are

largely unaffected by large (e.g., tidal) waves, but are only sensitive to the wind-driven centimeter-size capillary waves, and in this way distinguish them from other parts of the ocean wave spectra.

Both ocean surface currents and near-surface wind fields can be successfully retrieved using radar observations. While ground-based radar observations are largely limited by the straight view requirement, which restricts their use to near-coastline areas, airborne radar technology is partially free of the above limitations. With the enhancement of light aircraft technology, the measurement opportunities provided by airborne radars continuously increase and will likely continue to do so in the near future.

The near-surface wind vector over the ocean can be successfully estimated using scatterometric measurement techniques [1,2]. The scatterometer determines the normalized radar cross section (NRCS) of the observed surface and provides a retrieval of the wind vector parameters above it with the help of specialized geophysical model functions (GMFs) that relate the measured NRCS  $\sigma^\circ(U, \theta, \alpha)$ , wind speed  $U$ , incidence angle  $\theta$ , and azimuth illumination angle  $\alpha$  relative to the up-wind direction and other environmental parameters. For operational use, the GMFs are represented in various forms. One of these forms is [3]:

$$\sigma^\circ(U, \theta, \alpha) = A(U, \theta) + B(U, \theta) \cos \alpha + C(U, \theta) \cos(2\alpha), \quad (1)$$

where  $A(U, \theta)$ ,  $B(U, \theta)$ , and  $C(U, \theta)$  are the coefficients, which are  $A(U, \theta) = a_0(\theta)U^{\gamma_0(\theta)}$ ,  $B(U, \theta) = a_1(\theta)U^{\gamma_1(\theta)}$ , and  $C(U, \theta) = a_2(\theta)U^{\gamma_2(\theta)}$ ;  $a_0(\theta)$ ,  $a_1(\theta)$ ,  $a_2(\theta)$ ,  $\gamma_0(\theta)$ ,  $\gamma_1(\theta)$ , and  $\gamma_2(\theta)$  are the coefficients dependent on the incidence angle, radar wave length, and polarization.

The backscattering from the ocean surface depends on both the wind speed and direction. Therefore, this feature can be used for the retrieval of the near-surface wind vector. This estimation process is performed by a so-called model function inversion that appears as a complex nonlinear procedure, as one can easily see from Equation (1). The antenna configuration and the geometry of its beams are important factors for the scatterometer wind retrieval efficacy.

In earlier considerations, the use of different antenna configurations has been considered, including both fixed- and rotating antenna systems, with or without horizontal stabilization, with measurements performed during either circular or rectilinear flight [4–16]. While our previous research largely focused on the possibility of using various existing onboard equipment for overall cost reduction [17–20], no systematic comparison of both the accuracy and performance of the measurement algorithms for different antenna configurations has been done.

However, nowadays, after long-term periods of increase in fuel price and the decrease of electronic equipment costs, it appears plausible to use specially designed lightweight equipment that only need light aircraft to carry them. As modern phase antenna arrays are capable of effective adjustment of their configurations and beam geometries by software controlled spatial filtering, the choice of a particular option would rather be balanced by the potential accuracy and the requirements of computational power for the online analysis by onboard equipment or data storage or the transmission interface for offline analysis later on the ground.

As our earlier experience indicates, azimuthally diverse NRCS measurements are the best option for scatterometric measurements [17–20]. That is why wind scatterometers often have either single-beam rotating antennas or multi-beam fixed antenna geometries. In the case of tunable antenna arrays, the rotation of the antenna system can be effectively replaced by its consecutive electronic switching between closely displaced beams. Thus, both above configurations could be effectively generalized in a single multi-beam star geometry, where increase in the number of beams increases the angular resolution of the analysis finally converging to the scenario that is effectively equivalent to that provided by the single-beam rotating antenna. This way the use of tunable antenna arrays allows all that to be implemented as a single fixed piece of equipment with software controlled parameters.

Therefore, this research aims to investigate the GMF analysis and the choice of the most suitable geometry for the airborne multi-beam scatterometers.



configuration for such an application was the X-configuration, with the same azimuthal angles between the nearest beams that is identical to the four-beam star geometry.

To investigate the applicability of the star geometry of beams and feasibility of the wind retrieval procedure proposed for a scatterometer, simulations have been performed for a various number of the antenna beams orientated as a star in the azimuthal plane. The GMF for the horizontal transmitting and receiving polarization from [21], with the following coefficients:

$$\begin{aligned} a_0(\theta) &= 10^{2.47324-0.22478\theta+0.001499\theta^2}, & a_1(\theta) &= 10^{-0.50593-0.11694\theta+0.000484\theta^2}, \\ a_2(\theta) &= 10^{1.63685-0.2100488\theta+0.001383\theta^2}, & \gamma_0(\theta) &= -0.15 + 0.071\theta - 0.0004\theta^2, \\ \gamma_1(\theta) &= -0.02 + 0.061\theta - 0.0003\theta^2, & \gamma_2(\theta) &= -0.16 + 0.074\theta - 0.0004\theta^2 \end{aligned}$$

have been used for the inversion procedure, as well as a Rayleigh Power (Exponential) distribution, which has been applied to simulate the “measured” NRCSs. An evaluation of the accuracy of both the wind speed and direction recovery has been performed using Monte Carlo simulations for wind speeds ranging from 2 to 20 m/s, with 30 independent trials for each wind speed and each geometric configuration.

To evaluate the wind retrieval at medium incidence angles, the simulations have been performed for three such incidence angles, in particular 30°, 45°, and 60°. Simulations for different numbers of beams have been performed such that the total number of the “measured” NRCS samples obtained by all beams in the considered star configuration was either identical or very close to each other, in particular 20000 for the 30° incidence angle, and 6260 at the incidence angles of 45° or 60°. A higher number of NRCS samples used at the 30° incidence angle is required due to the lower sensitivity for the wind retrieval at that incidence angle compared with higher incidence angles [19]. The results are shown for either no instrumental noise or with 0.1 dB noise at the incidence angle of 30° and 0.2 dB noise at the incidence angles of 45° and 60°.

For a four-beam star geometry ( $N = 4$ ) with the beam directions of 0°, 90°, 180°, and 270° relative to the aircraft course, the number of “measured” NRCS samples averaged for each beam is 5000 at the incidence angle of 30° and 1565 at the incidence angles of 45° or 60°. Our simulations have shown that without instrumental noise, the maximum errors of the wind speed and direction retrieval are 0.37 m/s and 10.3°, 0.57 m/s and 4.8°, and 0.48 m/s and 5.4°, respectively, at the incidence angles of 30°, 45°, and 60°. The simulation results with the instrumental noise assumption of 0.1 dB and 0.2 dB are summarized in Figures 1–3, respectively. Here, the maximum errors were 0.39 m/s and 16.2°, 0.58 m/s and 7.2°, and 0.49 m/s and 6.2°, respectively, at the incidence angles of 30°, 45°, and 60°.

Similar simulation results for the intermediate configurations with  $N = 5, 6, 8, 10, 12, 18$ , and 36 beam geometries are provided in detail in Appendix A. At the other end stands the seventy-two-beam star geometry ( $N = 72$ ), with the equiangular beams directed with a 5° increment angle that is comparable with a typical antenna beam angular resolution and thus should represent a scenario close to the electronically “rotating” antenna system. Particular measurement angles, in this case, are 0°, 5°, 10°, ..., 355° relative to the aircraft course, with the number of “measured” NRCS samples averaged for each beam being 278 at the incidence angle of 30°, and 87 at the incidence angles of 45° or 60°. The simulations without instrumental noise have shown the maximum errors of the wind speed and direction retrieval of 0.31 m/s and 2.8°, 0.46 m/s and 4.3°, and 0.49 m/s and 3.4°, respectively, at the incidence angles of 30°, 45°, and 60°. The simulation results with the instrumental noise assumption of 0.1 dB and 0.2 dB are shown in Figures 4–6, respectively. The maximum errors are 0.32 m/s and 2.9°, 0.47 m/s and 4.5°, and 0.5 m/s and 3.5°, respectively, at the incidence angles of 30°, 45°, and 60°.



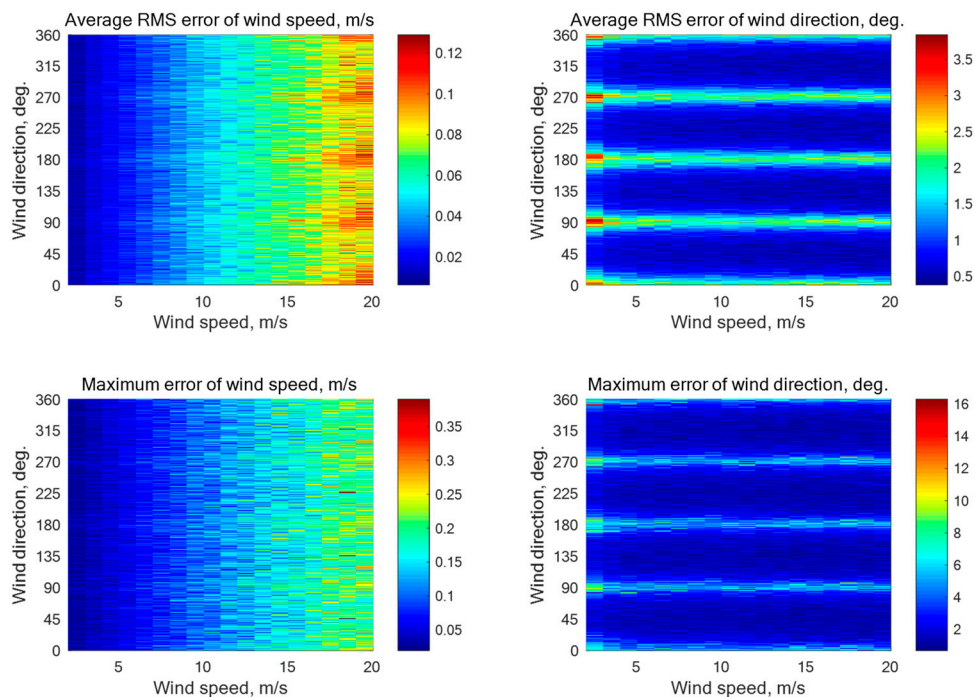


**Figure 1.** Simulation results for a four-beam star geometry ( $N = 4$ ) with the beam directions of  $0^\circ$ ,  $90^\circ$ ,  $180^\circ$ , and  $270^\circ$  relative to the aircraft course with an assumption of 0.1 dB instrumental noise at the wind speeds of 2–20 m/s for the incidence angle of  $30^\circ$  with 5000 averaged NRCS samples for each azimuthal angle.

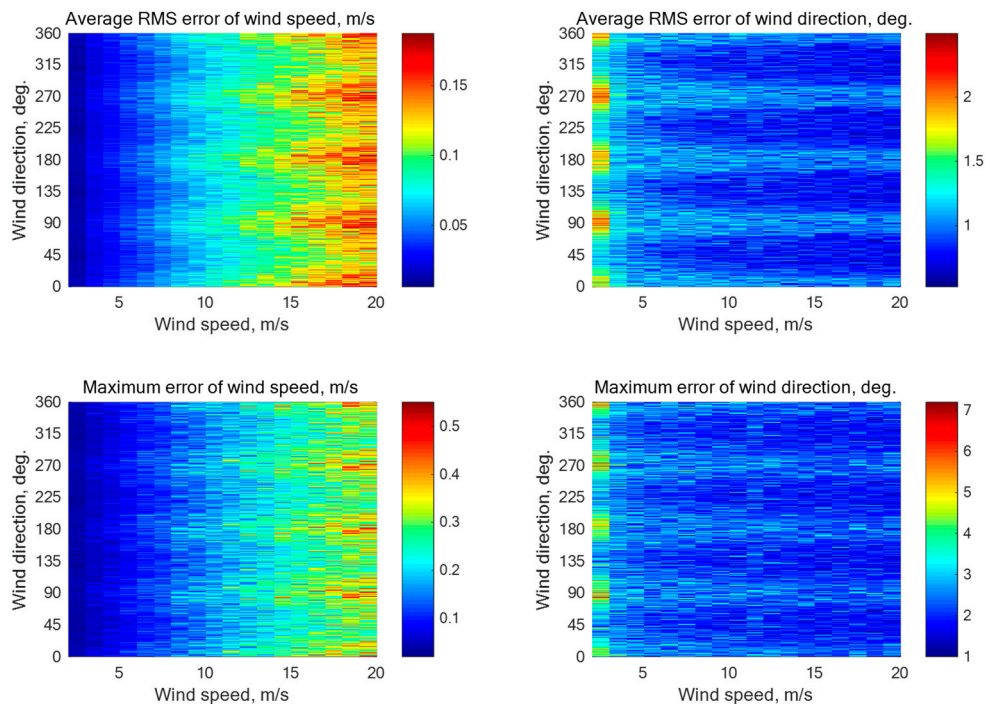


**Figure 2.** Simulation results for a four-beam star geometry ( $N = 4$ ) with the beam directions of  $0^\circ$ ,  $90^\circ$ ,  $180^\circ$ , and  $270^\circ$  relative to the aircraft course with an assumption of 0.2 dB instrumental noise at the wind speeds of 2–20 m/s for the incidence angle of  $45^\circ$  with 1565 averaged NRCS samples for each azimuthal angle.

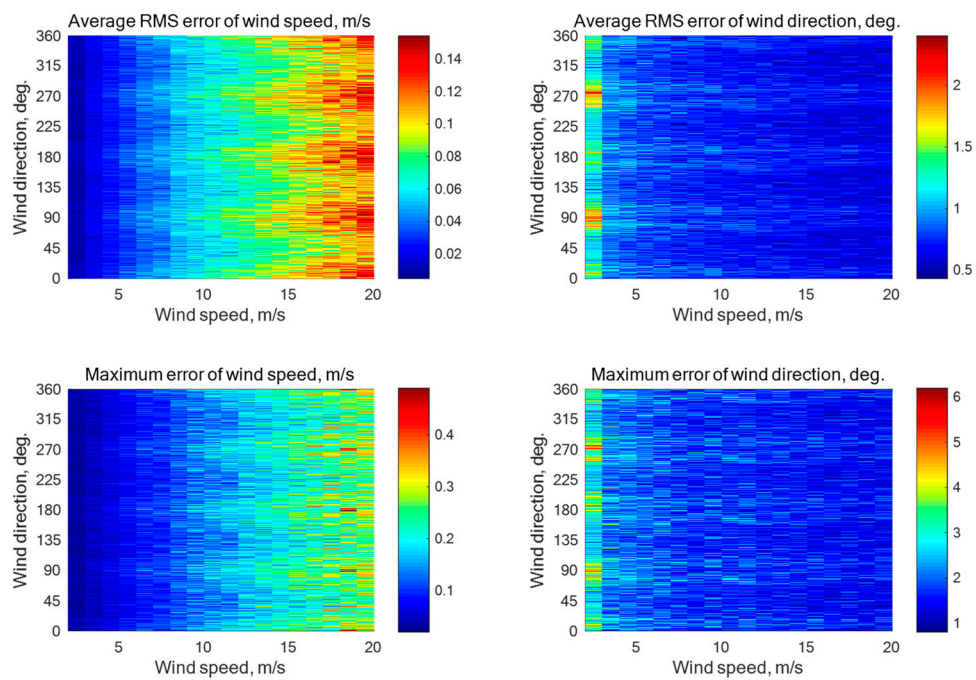


**Figure 3.** Simulation results for a four-beam star geometry ( $N = 4$ ) with the beam directions of  $0^\circ$ ,  $90^\circ$ ,  $180^\circ$ , and  $270^\circ$  relative to the aircraft course with an assumption of 0.2 dB instrumental noise at the wind speeds of 2–20 m/s for the incidence angle of  $60^\circ$  with 1565 averaged NRCS samples for each azimuthal angle.

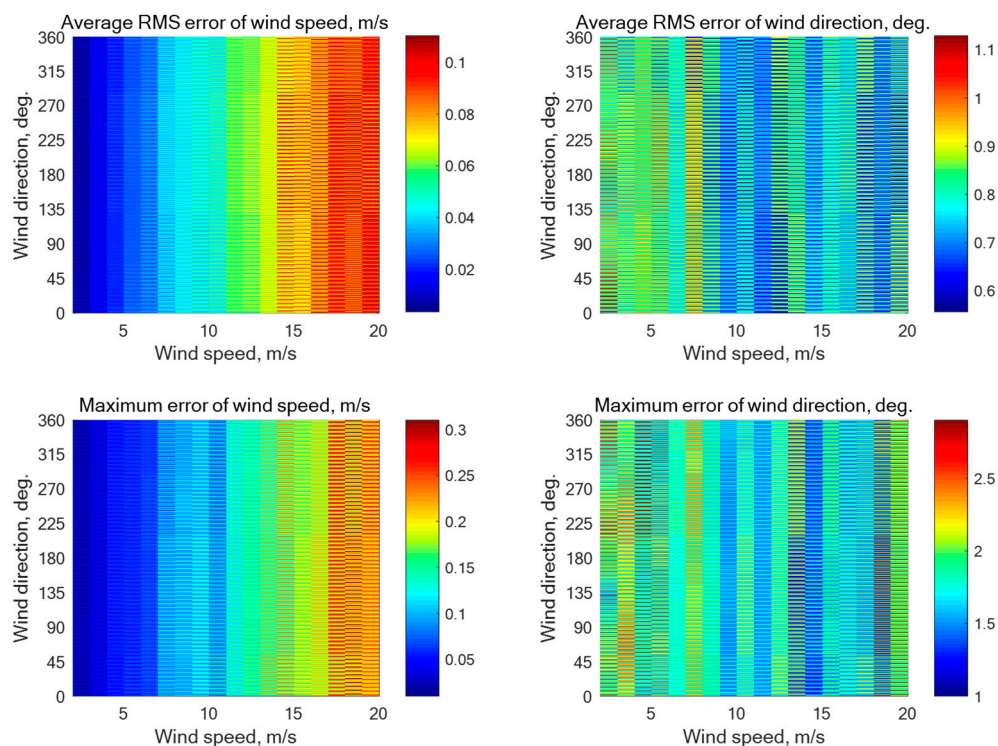


**Figure 4.** Simulation results for a 72-beam star geometry ( $N = 72$ ) with the beam directions of 0 to  $355^\circ$  with a  $5^\circ$  increment relative to the aircraft course with an assumption of 0.1 dB instrumental noise at the wind speeds of 2–20 m/s for the incidence angle of  $30^\circ$  with 278 averaged NRCS samples for each azimuthal angle.

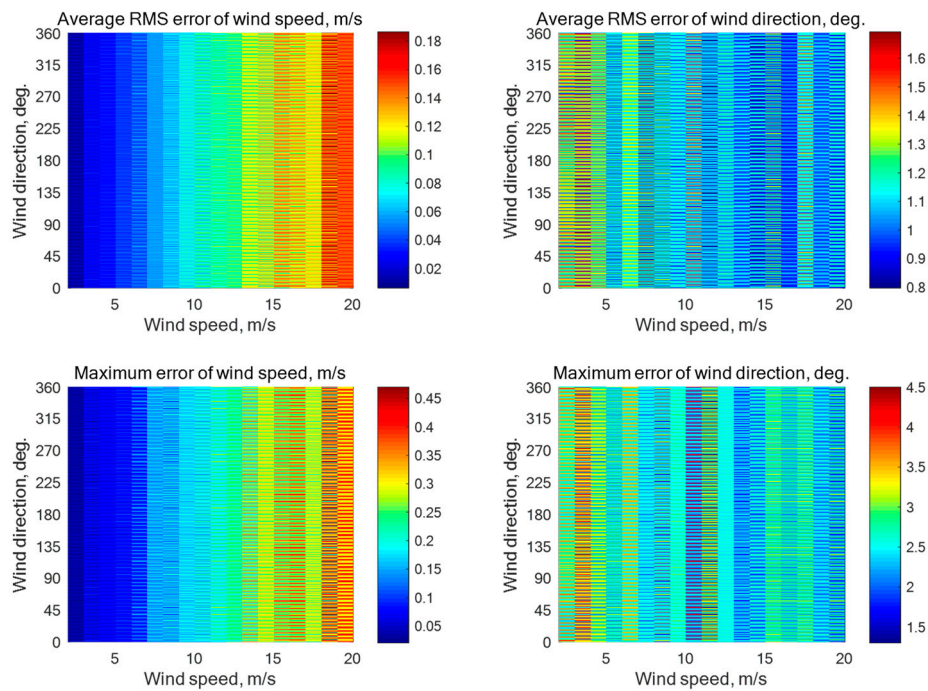


**Figure 5.** Simulation results for a 72-beam star geometry ( $N = 72$ ) with the beam directions of 0 to 355° with a 5° increment relative to the aircraft course with an assumption of 0.2 dB instrumental noise at the wind speeds of 2–20 m/s for the incidence angle of 45° with 87 averaged NRCS samples for each azimuthal angle.

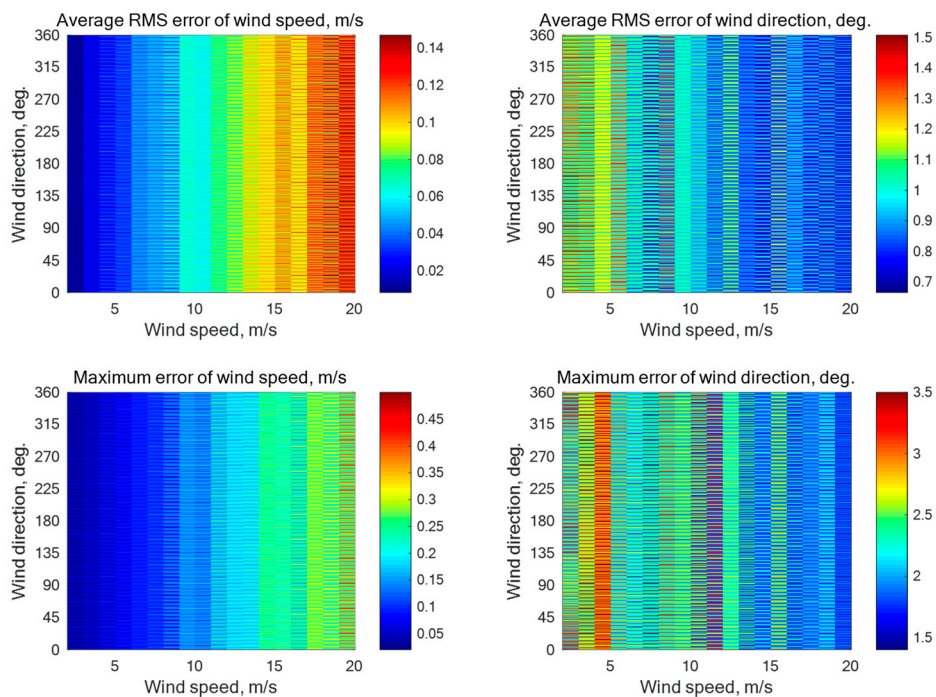


**Figure 6.** Simulation results for a 72-beam star geometry ( $N = 72$ ) with the beam directions of 0 to 355° with a 5° increment relative to the aircraft course with an assumption of 0.2 dB instrumental noise at the wind speeds of 2–20 m/s for the incidence angle of 60° with 87 averaged NRCS samples for each azimuthal angle.

The above results clearly indicate the suitability of a multi-beam star-configured geometry to measure a water-surface wind by an airborne scatterometer at medium incidence angles. The wind

speed and direction retrieval errors are within the ranges of a typical scatterometer wind measurement accuracy of  $\pm 2$  m/s and  $\pm 20^\circ$  [22], even in the worst case of the lower incidence angle of  $30^\circ$ . The wind speed error is lower at a lower wind speed and increases when the wind speed increases. At the same time, the wind direction error decreases with an increasing wind speed. The advantage of higher incidence angles can be attributed to the better appearance of the water-surface backscatter anisotropy at those angles of incidence [23]. Therefore, to reach the same wind retrieval accuracy, the required number of averaged NRCS samples at the incidence angle of  $30^\circ$  is larger than at  $45^\circ$  or  $60^\circ$ .

#### 4. Discussion

While the above diagrams provide complete information on the algorithm accuracy for all parameter combinations, in practical scenarios, there is no a priori information about the wind direction, and thus optimization must be performed for the arbitrarily chosen aircraft course. Therefore, let us next assume that  $\alpha$  can be any value between  $0^\circ$  and  $360^\circ$  with equal probability. In this case, it makes sense to consider the estimation error averaged over all azimuthal directions. The boxplots in Figures 7 and 8 for the corresponding Monte Carlo simulation results indicate that both the wind direction and speed estimates are unbiased, given that the error average and median are vanishing.

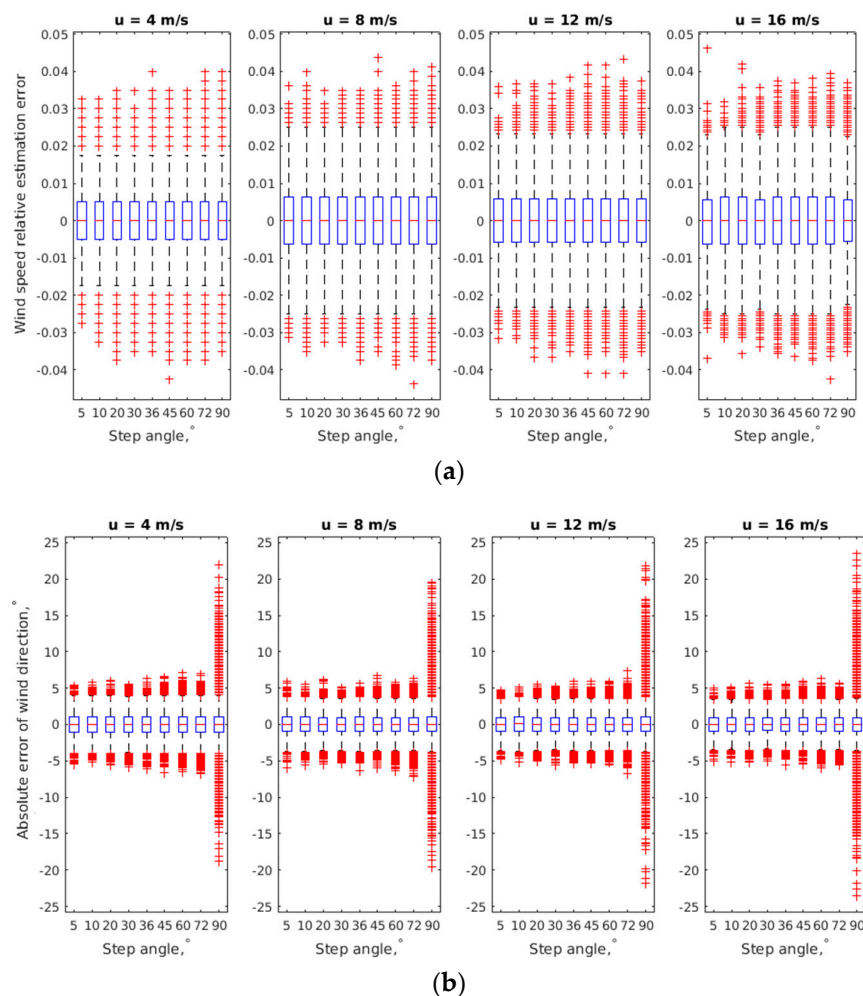


**Figure 7.** Wind direction (a) and speed estimation (b) errors for all considered antenna geometry configurations averaged over all azimuth angles assuming negligible instrumental measurement error. Data obtained by Monte-Carlo simulations with 1000 independent configurations for the incidence angle of  $30^\circ$  and the selected wind speeds of 4, 8, 12, and 16 m/s, respectively.



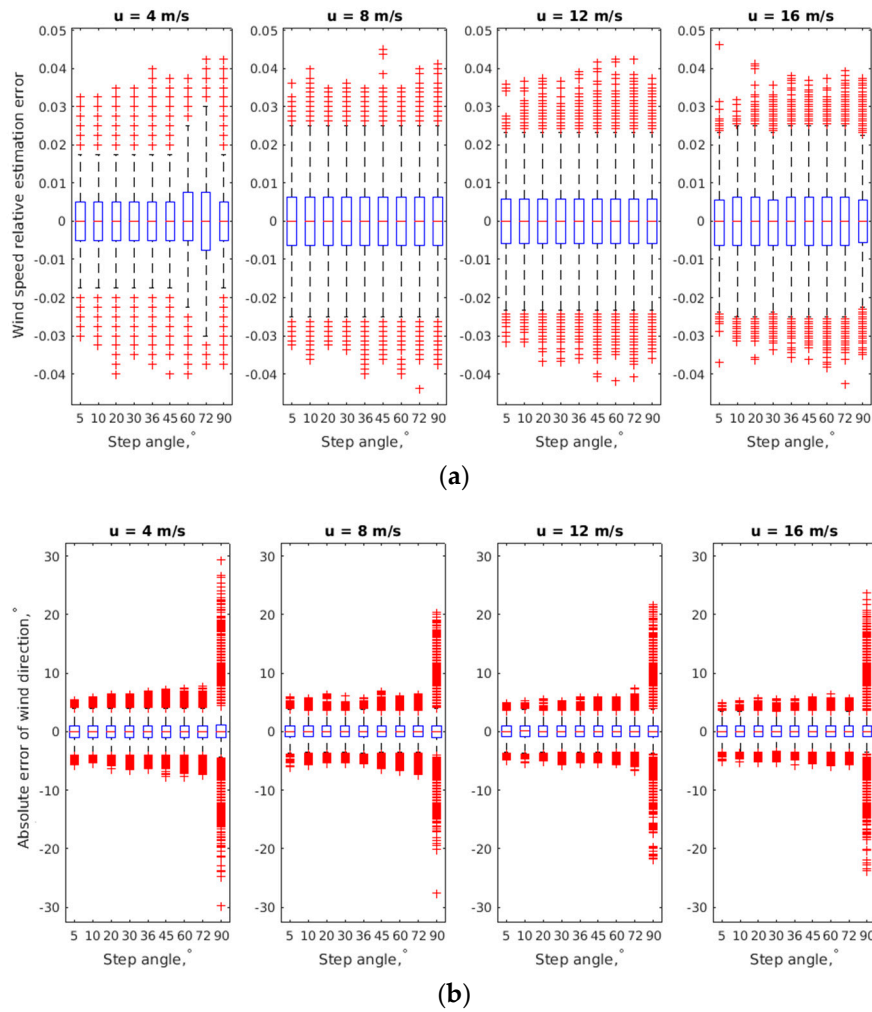


**Figure 8.** Wind direction (a) and speed estimation (b) errors for all considered antenna geometry configurations averaged over all azimuth angles assuming 0.1 dB instrumental measurement error. Data obtained by Monte-Carlo simulations with 1000 independent configurations for the incidence angle of 30° and the selected wind speeds of 4, 8, 12, and 16 m/s, respectively.

Next, interquartile and maximum wind speed estimation errors are all rather independent of the chosen antenna geometry configuration. In contrast, for the wind direction retrieval, the same holds only for the interquartile error, as the maximum error exhibits a moderate increase with decreasing the number of beams and this way decreasing the angular resolution of the antenna system. Remarkably, the four-beam configuration appears as an outlier with considerably heavier tails of the wind direction retrieval error distribution, while for five- and more beam configurations, increasing the number of beams leads to only a moderate decrease in the maximum error of the wind direction retrieval.

The simulation results presented above could be easily confirmed by the approximate treatment based on the quasi linear theory of error propagation. Given that the variance of two independent variables can be written as:

$$\begin{aligned}
 D\{\sigma^\circ\} &= \left[\frac{\partial G}{\partial U}\right]^2 D\{U\} + \left[\frac{\partial G}{\partial \alpha}\right]^2 D\{\alpha\} \\
 &= [a_0\gamma_0 U^{\gamma_0-1} + a_1\gamma_1 U^{\gamma_1-1} \cos(\alpha) + a_2\gamma_2 U^{\gamma_2-1} \cos(2\alpha)]^2 D\{U\} \\
 &\quad + [-a_1 U^{\gamma_1} \sin(\alpha) - 2a_2 U^{\gamma_2} \cos(2\alpha)]^2 D\{\alpha\}.
 \end{aligned} \tag{5}$$

The left part of Equation (5) is simply the variance of the averaged NRCS values. Since NRCS itself was simulated by a random exponentially distributed variable, it can be characterized by a single free parameter equal to its average that is in turn determined by the GMF (1).

Given that the variance of the exponential random variable equals its squared average and averaging of the  $N_s$  of its samples reduces the variance  $N_s$  times, the left part of Equation (5) yields:

$$D\{\sigma^\circ\} = \frac{[\sigma^\circ(U, \theta, \alpha)]^2}{N_s}, \quad (6)$$

where  $N_s$  is the total number of averaged samples given by the product of the number of antenna rays in a given antenna geometry configuration and the number of averaged samples in each beam. The variances of the azimuth illumination angle and wind speed in the right part of Equation (1) are the wind direction and wind speed estimation error variances, respectively, obtained by a series of 1000 Monte-Carlo simulations, as described above (also shown in Figures 7 and 8). To verify the results of the numerical treatment, we next calculated the ratio of the variances,  $D\{G\}/D\{\sigma^\circ\}$ , shown in Figure 9 (averaged over different azimuthal directions, like in Figures 7 and 8, respectively). The figure indicates that the results of the numerical treatment and approximations based on the quasi linear theory of error propagation agree, with the relative error remaining below 10% in all considered cases.

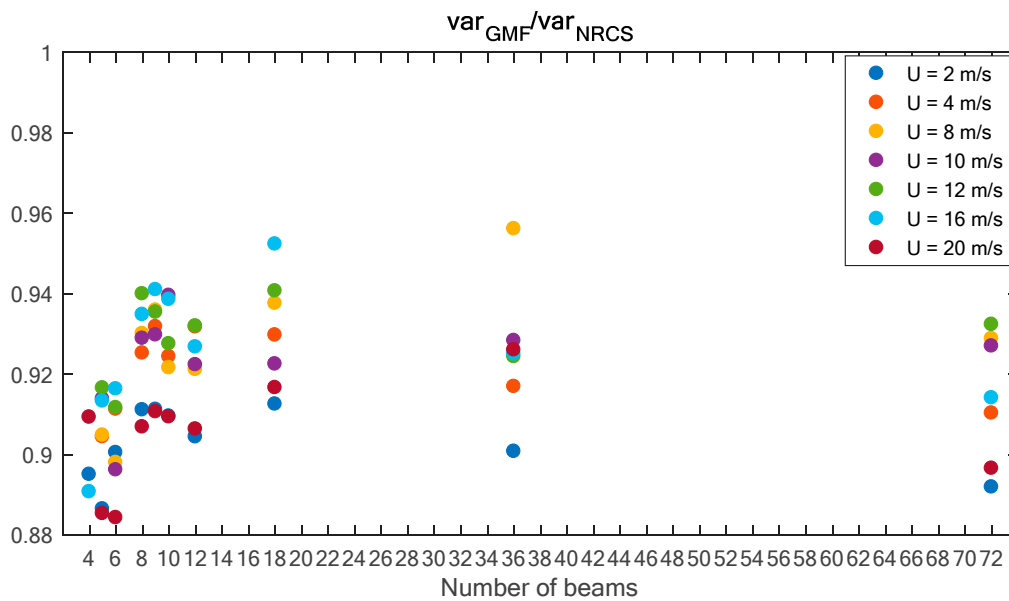


**Figure 9.** The ratio of the error variances  $D\{G\}/D\{\sigma^\circ\}$  obtained by numerical treatment and approximations based on the quasi linear theory of error propagation (averaged over different azimuthal directions, like in Figures 7 and 8, respectively).

The observed reduction in the maximum error comes at the cost of potentially more complex equipment that is capable of either the creation of complex multi-beam configurations, or rapidly switching between beam configurations by an electronically controlled tunable antenna array, this way simulating various multi-beam configurations. Another limitation arises from the computational complexity of the retrieval algorithm in which increasing the number of beams means also increasing the number of equations in the system of Equation (3). While the retrieval algorithm complexity is easily handled by current computational equipment available for post factum analysis, if the retrieval must be performed online using onboard computational tools, the required computational power may be a serious limitation.

Figure 10 shows the relative computational time of the wind vector retrieval algorithm. In the retrieval algorithm, the most computationally complex are matrix block multiplication operations that



increase as  $N^3$ , where  $N$  is the matrix dimension. However, there are also many other operations that increase slower with an increasing  $N$ , or even take fixed times independent of  $N$ . The figure shows that the overall computational complexity, and thus also computational time, increases asymptotically exponentially. Moreover, since complete simulation also includes steps, such as data generation and preparation, where the first is not required for real-time measurements, while the second could be partially resolved at the hardware level, we also provide the computational complexity statistics obtained exclusively for the retrieval algorithm using 1000 independent runs for each configuration. Accordingly, as indicated by our data, configurations with a large number of beams corresponding to a higher angular resolution, while providing more accurate measurements, may appear too costly in terms of their computational complexity, especially for the online analysis that has to be performed with onboard equipment. Based on the above data, depending on whether the measurements are provided online or can be analyzed post factum on the ground, one can consider choosing the best configuration in terms of accuracy vs computational complexity balance.

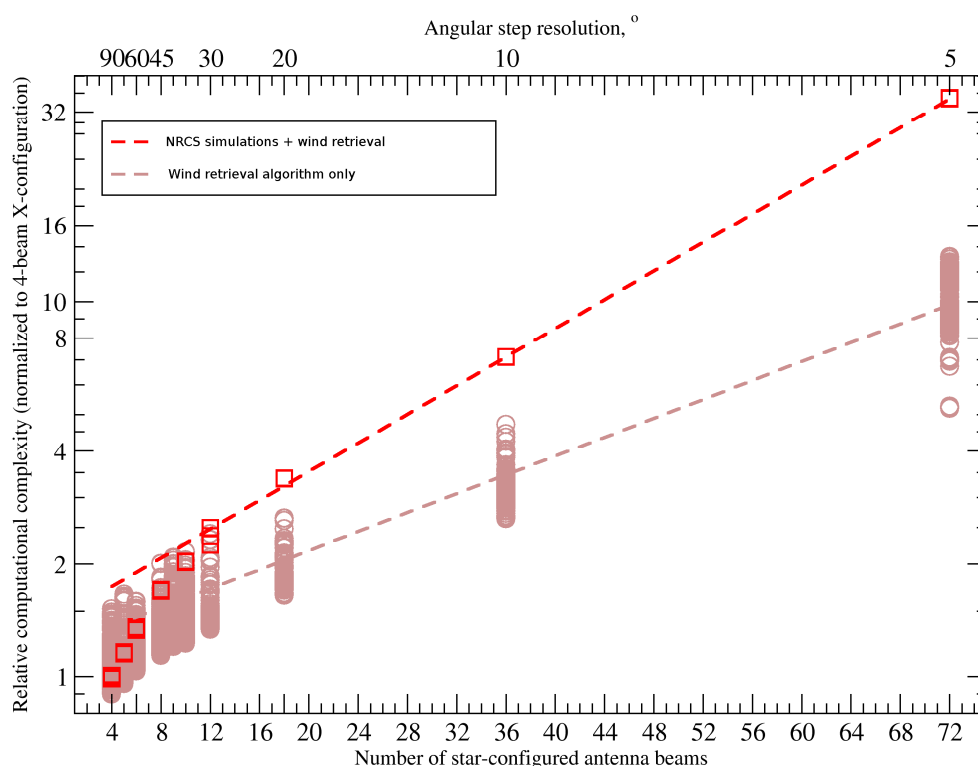


**Figure 10.** Relative computational times required by the wind vector retrieval algorithms normalized to the average times required by the simplest four-beam X-configuration. Circles show the results of 1000 test iterations of the retrieval algorithm only for each antenna geometry configuration, while the squares denote the total time taken by the entire simulation algorithm that contains both NRCS simulations and the wind retrieval algorithm. As the complexity of different parts of the algorithm increases differently with an increasing the number of beams, dashed lines showing exponential fits for the asymptotic behavior, indicating different asymptotic slopes.

At the same time, the measurement algorithm proposed also fits well for wind retrieval from the NRCS data set obtained by the typical airborne scatterometer with a single-beam rotated antenna at a rectilinear flight or with a fixed fan-beam antenna at a circular flight. The feasibility of such an application is supported by the results obtained for the 36- and 72-beam star geometries.

The altitude limitations for the multi-beam star-configured airborne scatterometer are determined by the dimensions of the area observed. Usually, it is considered that the sea area has identical wind and wave conditions when its dimensions do not exceed 15–20 km. If so, the maximum altitudes

for the wind retrieval at a one-stage measurement procedure are about 20, 10, and 5 km for beams' incidence angles of  $30^\circ$ ,  $45^\circ$ , and  $60^\circ$ , respectively.

The main recommendation for performing the wind retrieval is that the proposed measuring procedure requires a stable horizontal rectilinear flight when measurements are performed after establishing the given altitude and speed of flight. The measurement is finished when the needed number of NRCSs for each direction is obtained. When needed a greater number of NRCS samples for each direction observed can be obtained at several consecutive flights over the same area keeping the same course, altitude, and speed of flight in all the consecutive flights.

## 5. Conclusions

The analysis of multi-beam star-configured measurement geometries related to airborne scatterometer wind retrieval applications has demonstrated their feasibility. The measurement algorithm proposed can be applied not only for the wind measurements with the multi-beam scatterometers at rectilinear flight, but can also be used in the limiting case scenario with an airborne scatterometer having a single-beam antenna rotating either physically or electronically at a rectilinear flight or, equivalently, with an airborne scatterometer equipped with a fixed fan-beam antenna at a circular flight.

To provide unambiguous airborne wind measurements, at least four star-configured beams are required. The horizontal transmitter and receiver polarization providing the greatest difference between the up-wind and down-wind NRCSs as compared with the vertical polarization should be used [23]. The desirable incidence angles are within the range of medium incidence angles, in preference of the range between  $45^\circ$  and  $60^\circ$ , as it required a number of averaged NRCS samples about three times less than at  $30^\circ$  incidence angle.

Using Monte Carlo simulations for the fixed total measurement time, we have shown explicitly that among considered antenna configurations only the simplest X-configuration yields a considerably higher maximum error in the wind direction retrieval, while other errors remain comparable. The error reduction can be easily achieved by increasing the number of beams in the star geometry antenna configuration, this way increasing the angular resolution, while at the cost of considerable complication of the retrieval algorithm. Remarkably, the simplest X-configuration, while simplest in terms of hardware implementation and computational time, appears an outlier, yielding considerably higher maximum retrieval errors when compared to all other configurations. We believe that our results are useful for the optimization of both the hardware and software design for modern airborne scatterometric measurement systems based on tunable antenna arrays, especially those requiring online data processing.

The multi-beam star geometry, recommendations to perform the measurements, and algorithm proposed can be used for the development of new airborne radar sensors as well as for the functionality enhancement of current airborne radar systems providing aircraft navigation and avoidance [24,25]. Moreover, with the rapid development of UAV technology, we believe that light aircraft could be replaced by a similarly sized UAV as a radar system carrier, thus making it easier to run a measurement campaign. Additional benefits could be provided by combining measurements from ground- and airborne- based radars, including deep integration with signals emitted by the ground-based stations also received by the airborne stations and vice versa, that could be implemented by using similar electronically tunable antenna systems on both sides; thus, further enhancing the capabilities of the measurement systems. However, such a combination was beyond the scope of this current study.

**Author Contributions:** Conceptualization, A.N.; Methodology, A.N., A.K. and M.B.; Software, A.K. and E.A.; Validation, A.K., E.A., D.P. and M.B.; Formal Analysis, A.N. and V.O.; Investigation, A.N., A.K. and D.P.; Resources, V.V. and O.M.; Data Curation, A.K. and O.M.; Writing-Original Draft Preparation, A.N. and M.B.; Writing-Review & Editing, A.N., V.O., V.V. and M.B.; Visualization, A.K. and M.B.; Supervision, V.V., O.M. and M.B.; Project Administration, O.M. and M.B.; Funding Acquisition, V.V. and M.B.

**Funding:** This research was funded by the Russian Science Foundation grant number 16-19-00172. The APC was funded by the Russian Science Foundation grant number 16-19-00172.

**Acknowledgments:** A.N. wishes to express his sincere appreciation to Arne Jacob and Klaus Schünemann, both from the Hamburg University of Technology, for the provided opportunities and illuminating discussions during his exchange visit in the framework of the German Academic Exchange Service (DAAD) fellowship program.

**Conflicts of Interest:** The authors declare no conflict of interest. The funders had no role in the design of the study; in the collection, analyses, or interpretation of data; in the writing of the manuscript; and in the decision to publish the results.

## Appendix A

A five-beam star geometry ( $N = 5$ ) is characterized by the beam directions of  $0^\circ$ ,  $72^\circ$ ,  $144^\circ$ ,  $216^\circ$ , and  $288^\circ$  relative to the aircraft course. The number of “measured” NRCS samples averaged for each beam here is 4000 at the incidence angle of  $30^\circ$  and 1252 at the incidence angles of  $45^\circ$  or  $60^\circ$ . Simulations without additive instrumental noise have demonstrated the maximum errors of the wind speed and direction retrieval of 0.35 m/s and  $3.7^\circ$ , 0.64 m/s and  $5.0^\circ$ , and 0.5 m/s and  $5.4^\circ$ , respectively, at the incidence angles of  $30^\circ$ ,  $45^\circ$ , and  $60^\circ$ . Simulation results with the instrumental noise assumption of 0.1 dB and 0.2 dB are summarized in Figures A1–A3. The maximum errors are 0.36 m/s and  $6.0^\circ$ , 0.65 m/s and  $6.1^\circ$ , and 0.51 m/s and  $5.7^\circ$ , respectively, at the incidence angles of  $30^\circ$ ,  $45^\circ$ , and  $60^\circ$ .

For the six-beam star geometry ( $N = 6$ ) with the beam directions of  $0^\circ$ ,  $60^\circ$ ,  $120^\circ$ ,  $180^\circ$ ,  $240^\circ$ , and  $300^\circ$  relative to the aircraft course, the number of “measured” NRCS samples averaged for each beam is 3333 at the incidence angle of  $30^\circ$  and 1044 at the incidence angles of  $45^\circ$  or  $60^\circ$ . Simulations without instrumental noise have shown the maximum errors of the wind speed and direction retrieval of 0.35 m/s and  $3.5^\circ$ , 0.52 m/s and  $4.6^\circ$ , and 0.51 m/s and  $5.1^\circ$ , respectively, at the incidence angles of  $30^\circ$ ,  $45^\circ$ , and  $60^\circ$ . Simulation results with the instrumental noise assumption of 0.1 dB and 0.2 dB are summarized in Figures A4–A6. The maximum errors are 0.36 m/s and  $4.9^\circ$ , 0.53 m/s and  $5.8^\circ$ , and 0.52 m/s and  $5.3^\circ$  at the incidence angles of  $30^\circ$ ,  $45^\circ$ , and  $60^\circ$ , respectively.

The eight-beam star geometry ( $N = 8$ ) has the beam directions of  $0^\circ$ ,  $45^\circ$ ,  $90^\circ$ ,  $135^\circ$ ,  $180^\circ$ ,  $225^\circ$ ,  $270^\circ$ , and  $315^\circ$  relative to the aircraft course. The number of “measured” NRCS samples averaged for each beam is 2500 at the incidence angle of  $30^\circ$  and 783 at the incidence angles of  $45^\circ$  or  $60^\circ$ . The simulations without instrumental noise have shown the maximum errors of the wind speed and direction retrieval of 0.33 m/s and  $3.1^\circ$ , 0.53 m/s and  $5.0^\circ$ , and 0.47 m/s and  $4.2^\circ$ , respectively, at the incidence angles of  $30^\circ$ ,  $45^\circ$ , and  $60^\circ$ . The simulation results with the instrumental noise assumption of 0.1 dB and 0.2 dB are summarized in Figures A7–A9, respectively. The maximum errors are 0.34 m/s and  $4.9^\circ$ , 0.54 m/s and  $5.7^\circ$ , and 0.48 m/s and  $4.5^\circ$ , respectively, at the incidence angles of  $30^\circ$ ,  $45^\circ$ , and  $60^\circ$ .

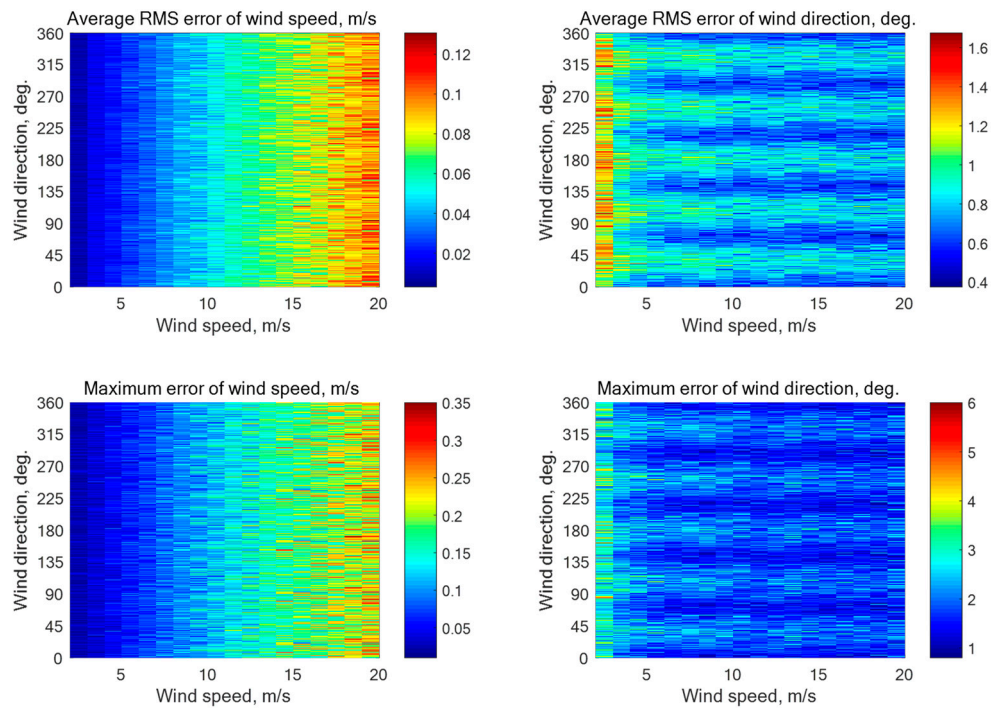


**Figure A1.** Simulation results for a five-beam star geometry ( $N = 5$ ) with the beam directions of  $0^\circ$ ,  $72^\circ$ ,  $144^\circ$ ,  $216^\circ$ , and  $288^\circ$  relative to the aircraft course with an assumption of 0.1 dB instrumental noise at the wind speeds of 2–20 m/s for the incidence angle of  $30^\circ$  with 4000 averaged NRCS samples for each azimuthal angle.

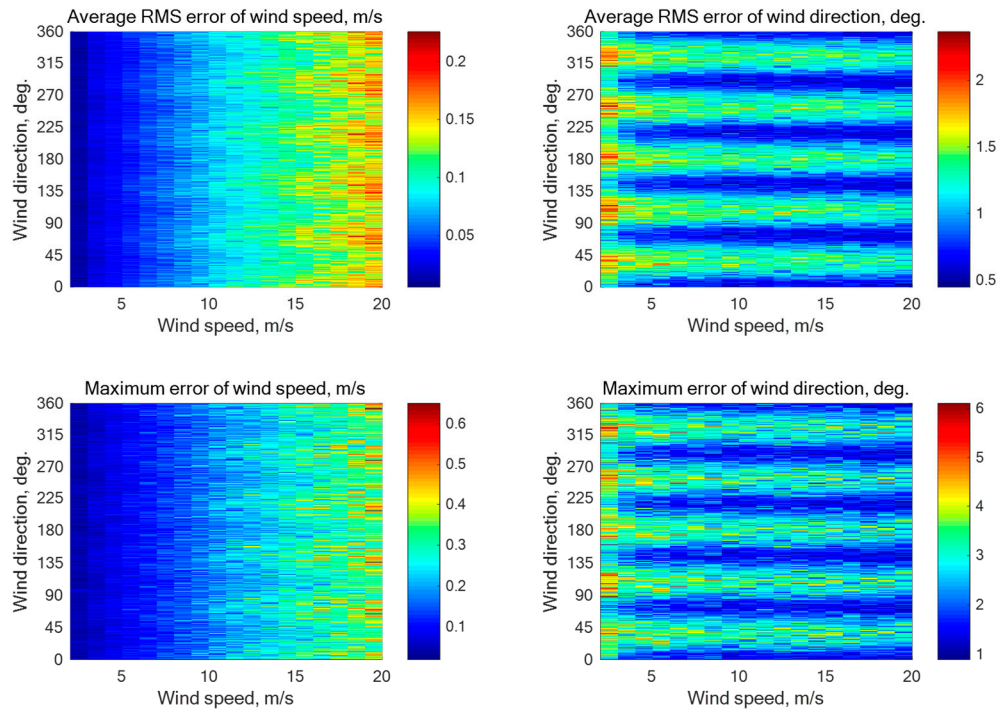


**Figure A2.** Simulation results for a five-beam star geometry ( $N = 5$ ) with the beam directions of  $0^\circ$ ,  $72^\circ$ ,  $144^\circ$ ,  $216^\circ$ , and  $288^\circ$  relative to the aircraft course with an assumption of 0.2 dB instrumental noise at the wind speeds of 2–20 m/s for the incidence angle of  $45^\circ$  with 1252 averaged NRCS samples for each azimuthal angle.

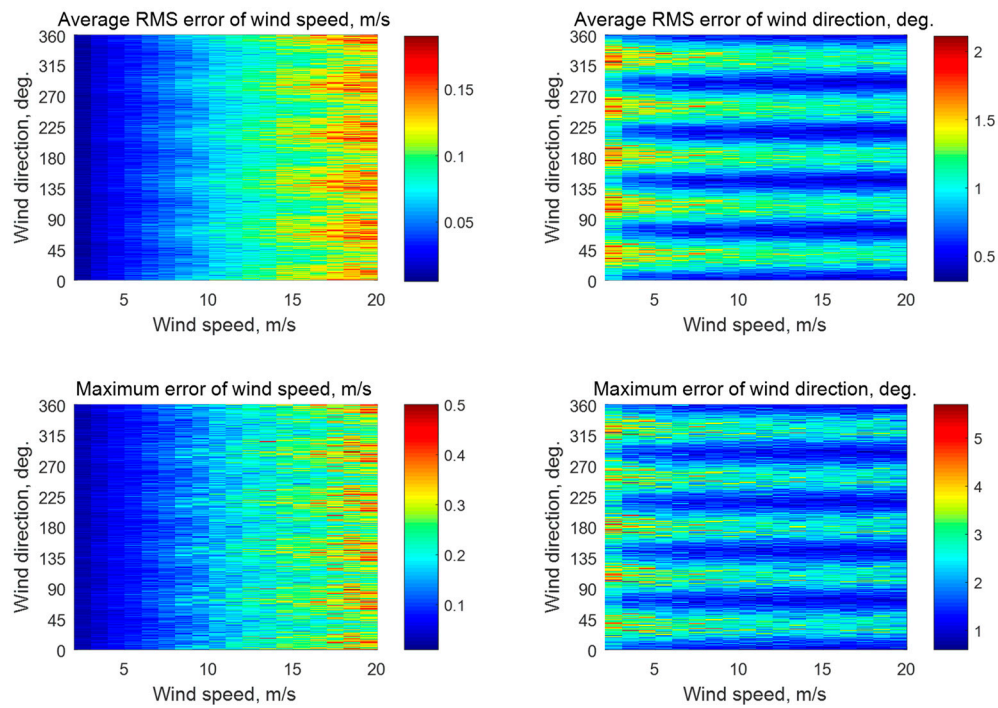


**Figure A3.** Simulation results for a five-beam star geometry ( $N = 5$ ) with the beam directions of  $0^\circ$ ,  $72^\circ$ ,  $144^\circ$ ,  $216^\circ$ , and  $288^\circ$  relative to the aircraft course with an assumption of 0.2 dB instrumental noise at the wind speeds of 2–20 m/s for the incidence angle of  $60^\circ$  with 1252 averaged NRCS samples for each azimuthal angle.

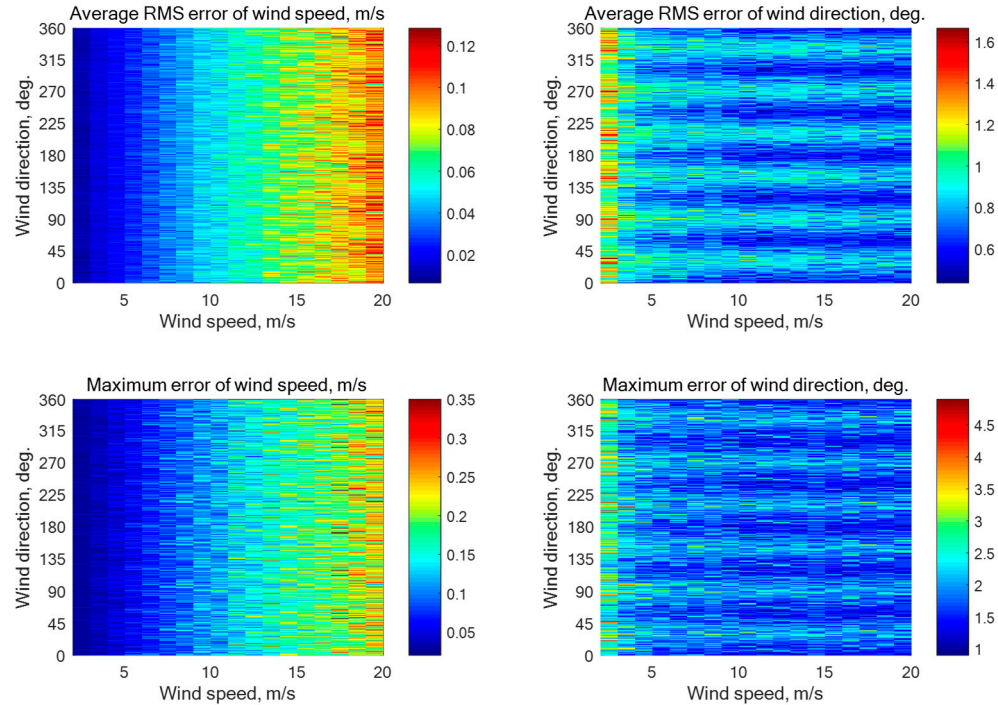


**Figure A4.** Simulation results for a six-beam star geometry ( $N = 6$ ) with the beam directions of  $0^\circ$ ,  $60^\circ$ ,  $120^\circ$ ,  $180^\circ$ ,  $240^\circ$ , and  $300^\circ$  relative to the aircraft course with an assumption of 0.1 dB instrumental noise at the wind speeds of 2–20 m/s for the incidence angle of  $30^\circ$  with 3333 averaged NRCS samples for each azimuthal angle.



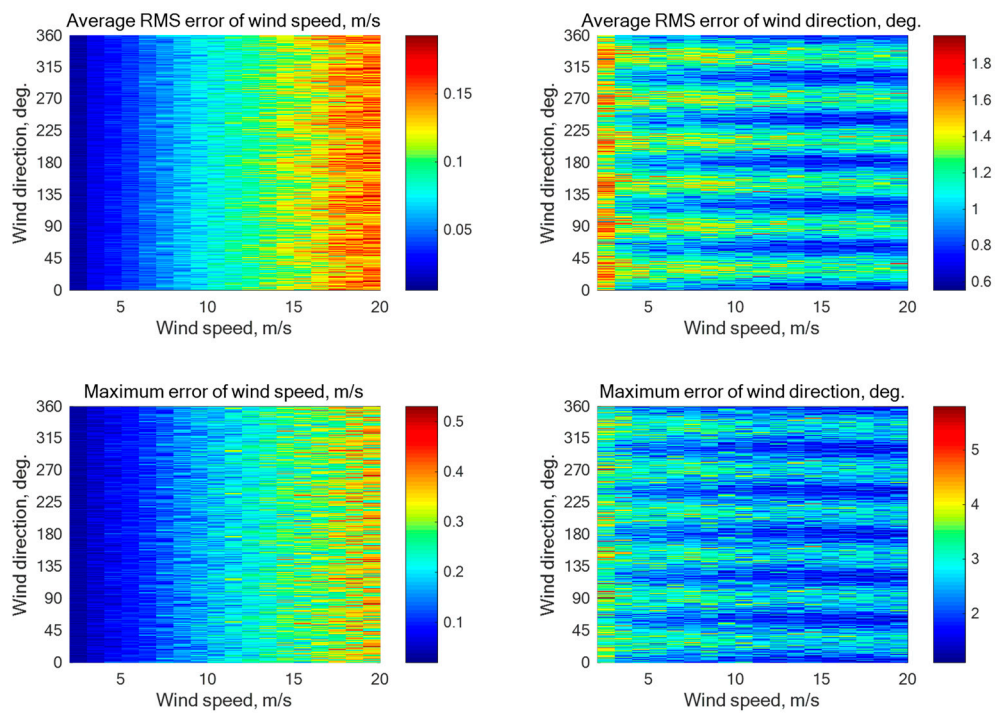


**Figure A5.** Simulation results for a six-beam star geometry ( $N = 6$ ) with the beam directions of  $0^\circ$ ,  $60^\circ$ ,  $120^\circ$ ,  $180^\circ$ ,  $240^\circ$ , and  $300^\circ$  relative to the aircraft course with an assumption of 0.2 dB instrumental noise at the wind speeds of 2–20 m/s for the incidence angle of  $45^\circ$  with 1044 averaged NRCS samples for each azimuthal angle.

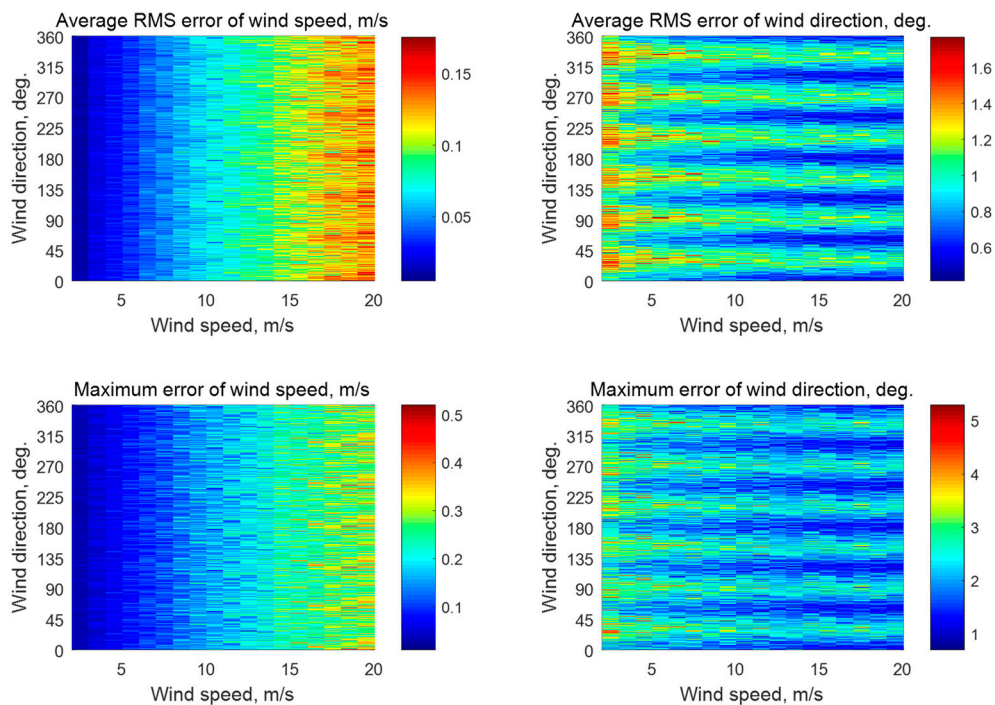


**Figure A6.** Simulation results for a six-beam star geometry ( $N = 6$ ) with the beam directions of  $0^\circ$ ,  $60^\circ$ ,  $120^\circ$ ,  $180^\circ$ ,  $240^\circ$ , and  $300^\circ$  relative to the aircraft course with an assumption of 0.2 dB instrumental noise at the wind speeds of 2–20 m/s for the incidence angle of  $60^\circ$  with 1044 averaged NRCS samples for each azimuthal angle.



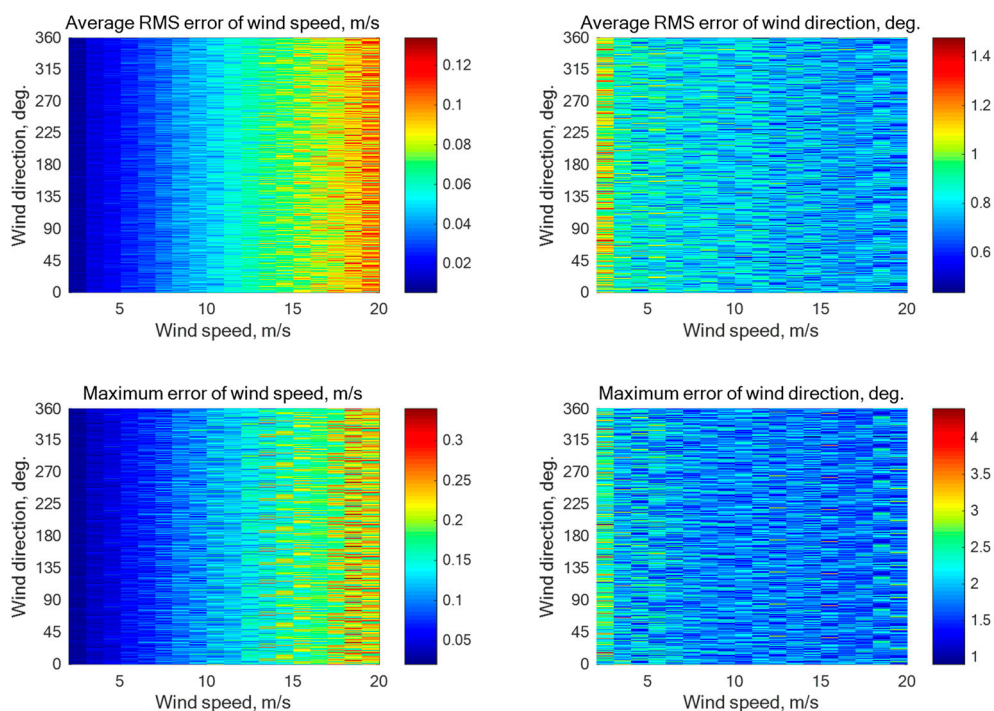


**Figure A7.** Simulation results for an eight-beam star geometry ( $N = 8$ ) with the beam directions of  $0^\circ$ ,  $60^\circ$ ,  $120^\circ$ ,  $180^\circ$ ,  $240^\circ$ , and  $300^\circ$  relative to the aircraft course with an assumption of 0.1 dB instrumental noise at the wind speeds of 2–20 m/s for the incidence angle of  $30^\circ$  with 2500 averaged NRCS samples for each azimuthal angle.

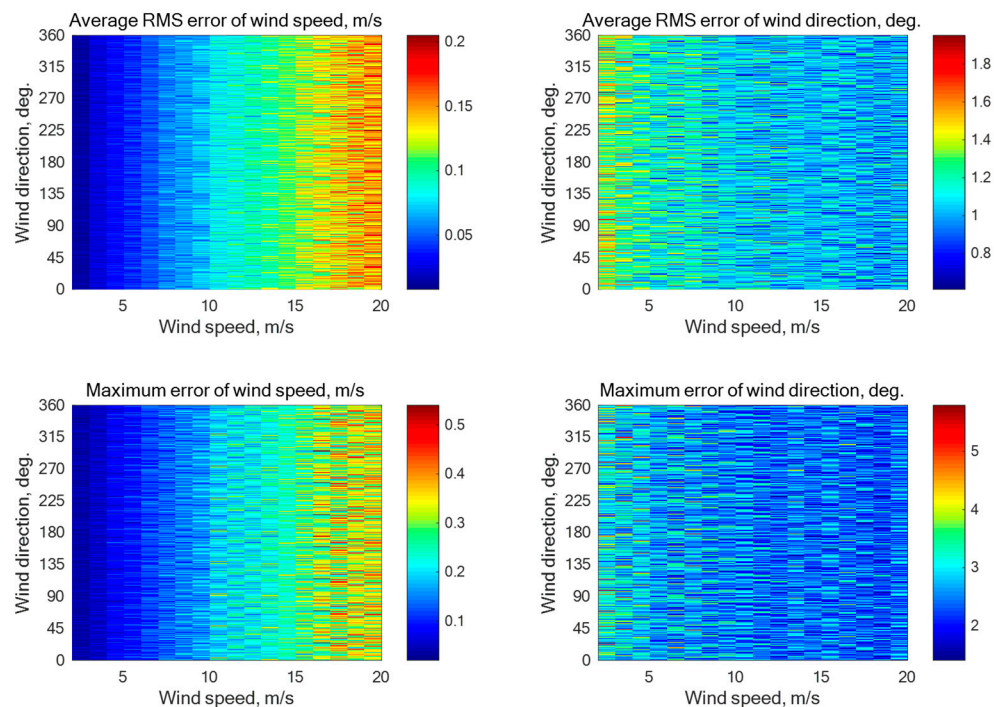


**Figure A8.** Simulation results for an eight-beam star geometry ( $N = 8$ ) with the beam directions of  $0^\circ$ ,  $60^\circ$ ,  $120^\circ$ ,  $180^\circ$ ,  $240^\circ$ , and  $300^\circ$  relative to the aircraft course with an assumption of 0.2 dB instrumental noise at the wind speeds of 2–20 m/s for the incidence angle of  $45^\circ$  with 783 averaged NRCS samples for each azimuthal angle.

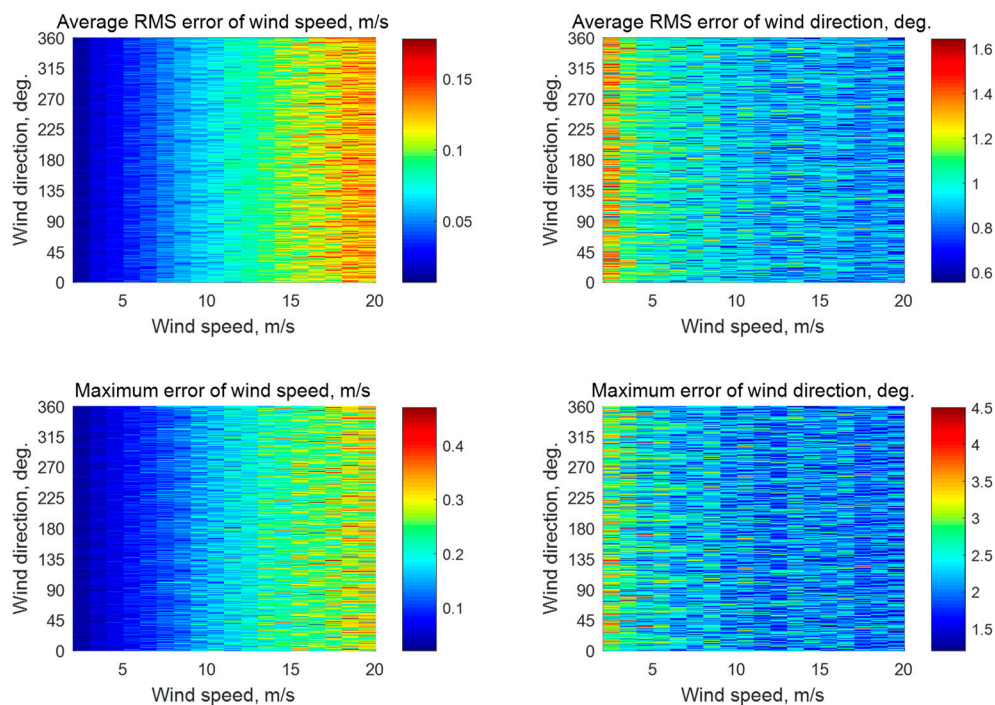


**Figure A9.** Simulation results for an eight-beam star geometry ( $N = 8$ ) with the beam directions of  $0^\circ$ ,  $60^\circ$ ,  $120^\circ$ ,  $180^\circ$ ,  $240^\circ$ , and  $300^\circ$  relative to the aircraft course with an assumption of 0.2 dB instrumental noise at the wind speeds of 2–20 m/s for the incidence angle of  $60^\circ$  with 783 averaged NRCS samples for each azimuthal angle.

For the ten-beam star geometry ( $N = 10$ ) with the beam directions of  $0^\circ$ ,  $36^\circ$ ,  $72^\circ$ ,  $108^\circ$ ,  $144^\circ$ ,  $180^\circ$ ,  $216^\circ$ ,  $252^\circ$ ,  $288^\circ$ , and  $324^\circ$  relative to the aircraft course, the number of “measured” NRCS samples averaged for each beam is 2000 at the incidence angle of  $30^\circ$  and 626 at the incidence angles of  $45^\circ$  or  $60^\circ$ . The simulations have shown that without instrumental noise the maximum errors of the wind speed and direction retrieval are 0.35 m/s and  $3.5^\circ$ , 0.53 m/s and  $4.6^\circ$ , and 0.48 m/s and  $3.9^\circ$ , respectively, at the incidence angles of  $30^\circ$ ,  $45^\circ$ , and  $60^\circ$ . The simulation results with the instrumental noise assumption of 0.1 dB and 0.2 dB are presented in Figures A10–A12, respectively. The maximum errors are 0.36 m/s and  $3.8^\circ$ , 0.54 m/s and  $5.7^\circ$ , and 0.49 m/s and  $4.8^\circ$ , respectively, at the incidence angles of  $30^\circ$ ,  $45^\circ$ , and  $60^\circ$ .

We have also performed simulations for twelve-beam geometry ( $N = 12$ ) and eighteen-beam geometry ( $N=18$ ). However, since in this range increasing  $N$  leads to a very small adjustment in the angular resolution, and all results were qualitatively similar such that no additional conclusions could be drawn, to save space, we skip the corresponding figures. Of note, results for twelve- and eighteen-beam geometries are nevertheless used in the summary boxplots in the main text (see Figure 7).

Next, a thirty-six-beam star geometry ( $N = 36$ ) characterized by the equiangular beams with a  $10^\circ$  increment angle, i.e.,  $0^\circ$ ,  $10^\circ$ ,  $20^\circ$ , ...,  $350^\circ$  relative to the aircraft course are considered. The number of “measured” NRCS samples averaged for each beam is 556 at the incidence angle of  $30^\circ$  and 174 at the incidence angles of  $45^\circ$  or  $60^\circ$ . The simulations without instrumental noise have demonstrated the maximum errors of the wind speed and direction retrieval of 0.28 m/s and  $3.0^\circ$ , 0.51 m/s and  $4.3^\circ$ , and 0.41 m/s and  $3.8^\circ$ , respectively, at the incidence angles of  $30^\circ$ ,  $45^\circ$ , and  $60^\circ$ . The simulation results with the instrumental noise assumption of 0.1 dB and 0.2 dB are presented in Figures A13–A15, respectively. The maximum errors are 0.29 m/s and  $3.1^\circ$ , 0.52 m/s and  $4.5^\circ$ , and 0.42 m/s and  $4.1^\circ$ , respectively, at the incidence angles of  $30^\circ$ ,  $45^\circ$ , and  $60^\circ$ .

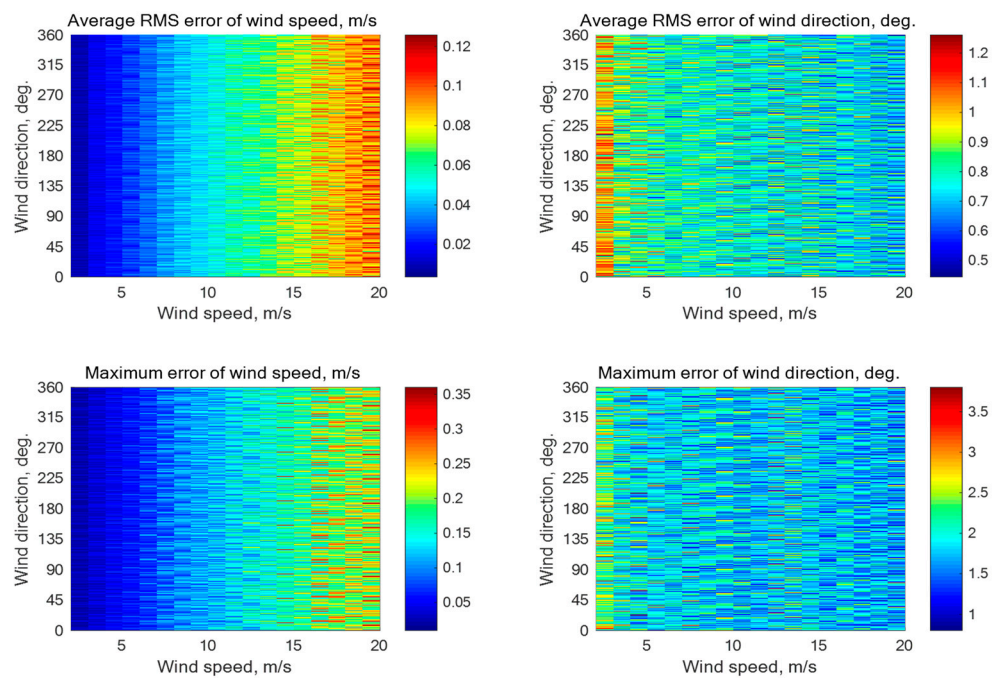


**Figure A10.** Simulation results for an eight-beam star geometry ( $N = 10$ ) with the beam directions of  $0^\circ, 36^\circ, 72^\circ, 108^\circ, 144^\circ, 180^\circ, 216^\circ, 252^\circ, 288^\circ,$  and  $324^\circ$  relative to the aircraft course with an assumption of 0.1 dB instrumental noise at the wind speeds of 2–20 m/s for the incidence angle of  $30^\circ$  with 2000 averaged NRCS samples for each azimuthal angle.

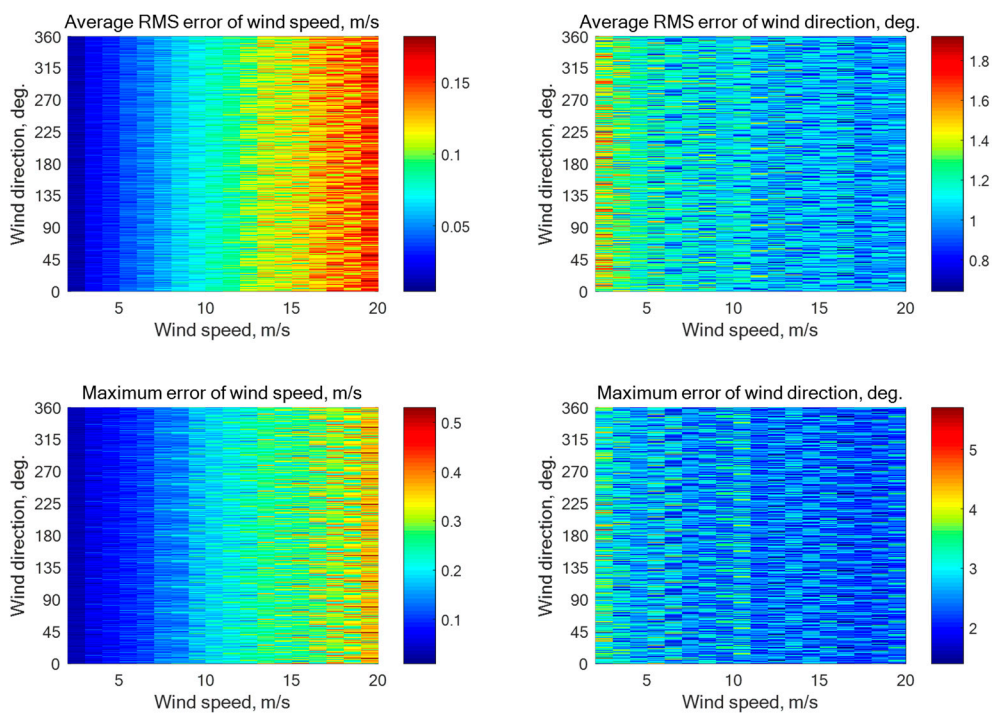


**Figure A11.** Simulation results for a ten-beam star geometry ( $N = 10$ ) with the beam directions of  $0^\circ, 36^\circ, 72^\circ, 108^\circ, 144^\circ, 180^\circ, 216^\circ, 252^\circ, 288^\circ,$  and  $324^\circ$  relative to the aircraft course with an assumption of 0.2 dB instrumental noise at the wind speeds of 2–20 m/s for the incidence angle of  $45^\circ$  with 626 averaged NRCS samples for each azimuthal angle.

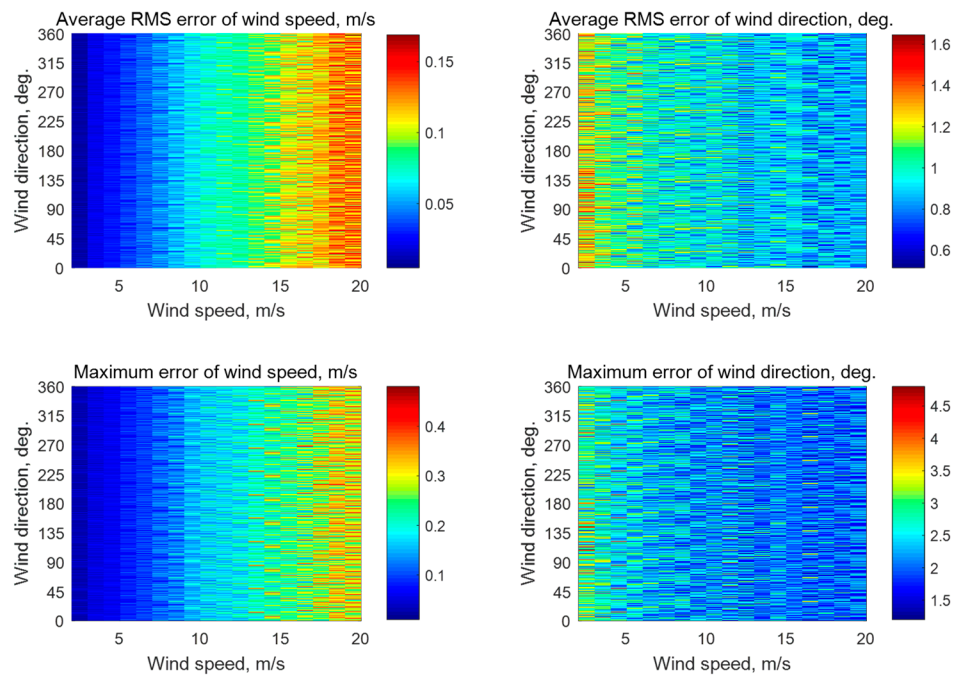


**Figure A12.** Simulation results for a ten-beam star geometry ( $N = 10$ ) with the beam directions of  $0^\circ$ ,  $36^\circ$ ,  $72^\circ$ ,  $108^\circ$ ,  $144^\circ$ ,  $180^\circ$ ,  $216^\circ$ ,  $252^\circ$ ,  $288^\circ$ , and  $324^\circ$  relative to the aircraft course with an assumption of 0.2 dB instrumental noise at the wind speeds of 2–20 m/s for the incidence angle of  $60^\circ$  with 626 averaged NRCS samples for each azimuthal angle.

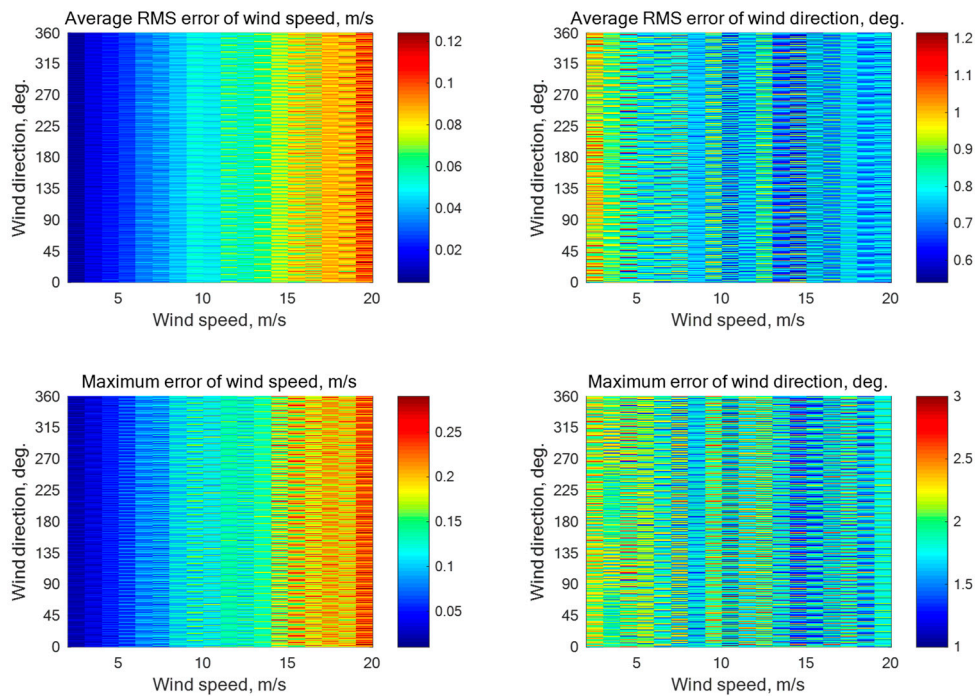


**Figure A13.** Simulation results for a thirty-six-beam star geometry ( $N = 36$ ) with the beam directions of  $0^\circ$ ,  $10^\circ$ ,  $20^\circ$ ,  $30^\circ$ ,  $40^\circ$ ,  $50^\circ$ ,  $60^\circ$ ,  $70^\circ$ ,  $80^\circ$ ,  $90^\circ$ ,  $100^\circ$ ,  $110^\circ$ ,  $120^\circ$ ,  $130^\circ$ ,  $140^\circ$ ,  $150^\circ$ ,  $160^\circ$ ,  $170^\circ$ ,  $180^\circ$ ,  $190^\circ$ ,  $200^\circ$ ,  $210^\circ$ ,  $220^\circ$ ,  $230^\circ$ ,  $240^\circ$ ,  $250^\circ$ ,  $260^\circ$ ,  $270^\circ$ ,  $280^\circ$ ,  $290^\circ$ ,  $300^\circ$ ,  $310^\circ$ ,  $320^\circ$ ,  $330^\circ$ ,  $340^\circ$ , and  $350^\circ$  relative to the aircraft course with an assumption of 0.1 dB instrumental noise at the wind speeds of 2–20 m/s for the incidence angle of  $30^\circ$  with 556 averaged NRCS samples for each azimuthal angle.



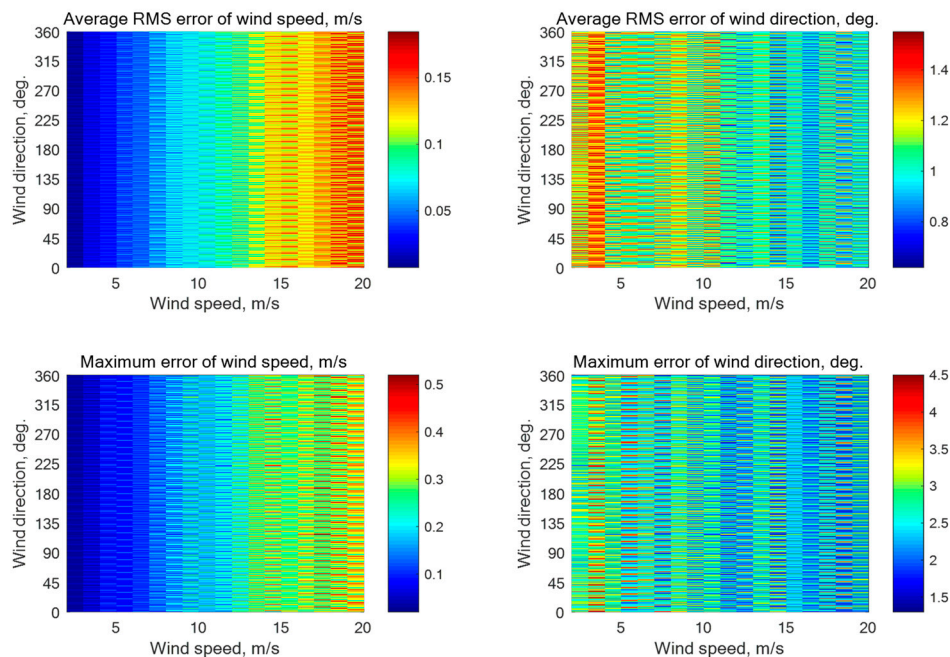


**Figure A14.** Simulation results for a thirty-six-beam star geometry ( $N = 36$ ) with the beam directions of  $0^\circ, 10^\circ, 20^\circ, 30^\circ, 40^\circ, 50^\circ, 60^\circ, 70^\circ, 80^\circ, 90^\circ, 100^\circ, 110^\circ, 120^\circ, 130^\circ, 140^\circ, 150^\circ, 160^\circ, 170^\circ, 180^\circ, 190^\circ, 200^\circ, 210^\circ, 220^\circ, 230^\circ, 240^\circ, 250^\circ, 260^\circ, 270^\circ, 280^\circ, 290^\circ, 300^\circ, 310^\circ, 320^\circ, 330^\circ, 340^\circ$ , and  $350^\circ$  relative to the aircraft course with an assumption of 0.2 dB instrumental noise at the wind speeds of 2–20 m/s for the incidence angle of  $45^\circ$  with 174 averaged NRCS samples for each azimuthal angle.

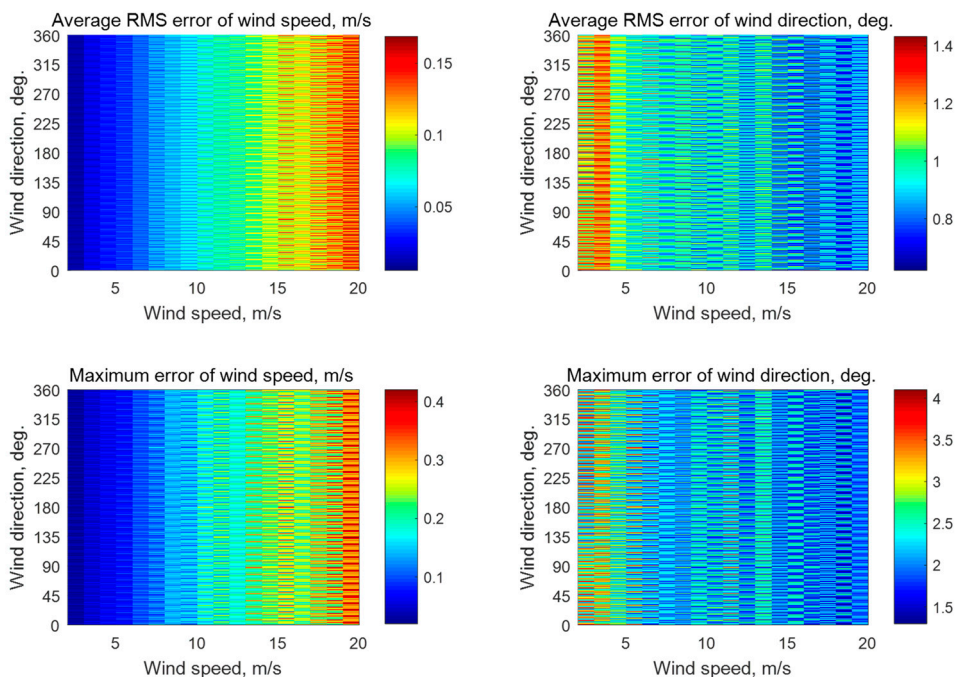


**Figure A15.** Simulation results for a thirty-six-beam star geometry ( $N = 36$ ) with the beam directions of  $0^\circ, 10^\circ, 20^\circ, 30^\circ, 40^\circ, 50^\circ, 60^\circ, 70^\circ, 80^\circ, 90^\circ, 100^\circ, 110^\circ, 120^\circ, 130^\circ, 140^\circ, 150^\circ, 160^\circ, 170^\circ, 180^\circ, 190^\circ, 200^\circ, 210^\circ, 220^\circ, 230^\circ, 240^\circ, 250^\circ, 260^\circ, 270^\circ, 280^\circ, 290^\circ, 300^\circ, 310^\circ, 320^\circ, 330^\circ, 340^\circ$ , and  $350^\circ$  relative to the aircraft course with an assumption of 0.2 dB instrumental noise at the wind speeds of 2–20 m/s for the incidence angle of  $60^\circ$  with 174 averaged NRCS samples for each azimuthal angle.

## References

1. Fung, A.K. *Backscattering from Multiscale Rough Surfaces with Application to Wind Scatterometry*; Artech House: Norwood, MA, USA, 2015; p. 328, ISBN 13:978-1-63081-000-9.
2. Nekrasov, A.; Dell'Acqua, F. Airborne Weather Radar: A theoretical approach for water-surface backscattering and wind measurements. *IEEE Geosci. Remote Sens. Mag.* **2016**, *16*, 38–50. [[CrossRef](#)]
3. Spencer, M.W.; Graf, J.E. The NASA scatterometer (NSCAT) mission. *Backscatter* **1997**, *8*, 18–24.
4. Moore, R.K.; Fung, A.K. Radar determination of winds at sea. *Proc. IEEE* **1979**, *67*, 1504–1521. [[CrossRef](#)]
5. Masuko, H.; Okamoto, K.; Shimada, M.; Niwa, S. Measurement of microwave backscattering signatures of the ocean surface using X band and Ka band airborne scatterometers. *J. Geophys. Res. Oceans* **1986**, *91*, 13065–13083. [[CrossRef](#)]
6. Wismann, V. Messung der Windgeschwindigkeit über dem Meer mit einem flugzeuggetragenen 5.3 GHz Scatterometer. Ph.D. Thesis, Universität 472 Bremen, Bremen, Germany, 1989; p. 119 S. (In German)
7. Hildebrand, P.H. Estimation of sea-surface wind using backscatter cross-section measurements from airborne research weather radar. *IEEE Trans. Geosci. Remote Sens.* **1994**, *32*, 110–117. [[CrossRef](#)]
8. Carswell, J.R.; Carson, S.C.; McIntosh, R.E.; Li, F.K.; Neumann, G.; McLaughlin, D.J.; Wilkerson, J.C.; Black, P.G.; Nghiem, S.V. Airborne scatterometers: Investigating ocean backscatter under low-and high-wind conditions. *Proc. IEEE* **1994**, *82*, 1835–1860. [[CrossRef](#)]
9. Kramer, H.J. *Observation of the Earth and its Environment: Survey of Missions and Sensors*, 4th ed.; Springer: Berlin, Germany, 2002.
10. Jones, W.L. Progress in scatterometer application. *J. Oceanogr.* **2002**, *58*, 121–136.
11. Karaev, V.Y.; Kanevsky, M.B.; Balandina, G.N.; Meshkov, E.M.; Challenor, P.; Srokosz, M.; Gommenginger, C. A rotating knife-beam altimeter for wide-swath remote sensing of ocean: Wind and waves. *Sensors* **2006**, *6*, 620–642. [[CrossRef](#)]
12. Njoku, E.G. *Encyclopedia of Remote Sensing*; Springer: New York, NY, USA, 2014; p. 939, ISBN 978-0-387-36698-2.
13. Fois, F.; Hoogeboom, P.; Le Chevalier, F.; Stoffelen, A. Future ocean scatterometry: On the use of cross-polar scattering to observe very high winds. *IEEE Trans. Geosci. Remote Sens.* **2015**, *53*, 5009–5020. [[CrossRef](#)]
14. Karaev, V.; Panfilova, M.; Titchenko, Y.; Meshkov, E.; Balandina, G. Retrieval of the near-surface wind velocity and direction: SCAT-3 orbit-borne scatterometer. *Radiophys. Quantum Electron.* **2016**, *59*, 259–269. [[CrossRef](#)]
15. Hauser, D.; Tison, C.; Amiot, T.; Delaye, L.; Corcoral, N.; Castellan, P. SWIM: The first spaceborne wave scatterometer. *IEEE Trans. Geosci. Remote Sens.* **2017**, *55*, 3000–3014. [[CrossRef](#)]
16. Rodríguez, E.; Wineteer, A.; Perkovic-Martin, D.; Gál, T.; Stiles, B.W.; Niamsuwan, N.; Rodríguez Monje, R. Estimating ocean vector winds and currents using a Ka-band pencil-beam Doppler scatterometer. *Remote Sens.* **2018**, *10*, 576. [[CrossRef](#)]
17. Nekrasov, A. On airborne measurement of the sea surface wind vector by a scatterometer (altimeter) with a nadir-looking wide-beam antenna. *IEEE Trans. Geosci. Remote Sens.* **2002**, *40*, 2111–2116. [[CrossRef](#)]
18. Nekrasov, A.; Khachatryan, A.; Veremyev, V.; Bogachev, M. Sea surface wind measurement by airborne weather radar scanning in a wide-size sector. *Atmosphere* **2016**, *7*, 72. [[CrossRef](#)]
19. Nekrasov, A.; Khachatryan, A.; Veremyev, V.; Bogachev, M. Sea wind measurement by Doppler navigation system with x-configured beams at rectilinear flight. *Remote Sens.* **2017**, *17*, 887. [[CrossRef](#)]
20. Khachatryan, A.; Nekrasov, A.; Bogachev, M. Sea wind parameters retrieval using Y-configured Doppler navigation system data. Performance and accuracy. *J. Phys. Conf. Ser.* **2018**, *1015*, 032058. [[CrossRef](#)]
21. Hans, P. Auslegung und Analyse von satellitengetragenen Mikrowellensensorsystemen zur Windfeldmessung (Scatterometer) über dem Meer und Vergleich der Meßverfahren in Zeit- und Frequenzebene. Von der Fakultät 2 Bauingenieur- und Vermessungswesen der Universität Stuttgart zur Erlangung der Würde eines Doktor-Ingenieurs genehmigte Abhandlung. Ph.D. Thesis, Institut für Navigation der Universität Stuttgart, Stuttgart, Germany, 1987; p. 225 S. (In German)
22. Komen, G.J.; Cavaleri, L.; Donelan, M.; Hasselmann, K.; Hasselmann, S.; Janssen, P.A.E.M. *Dynamics and Modelling of Ocean Waves*; Cambridge University Press: Cambridge, UK, 1994; p. 532.
23. Ulaby, F.T.; Moore, R.K.; Fung, A.K. *Microwave Remote Sensing: Active and Passive, Volume II: Radar Remote Sensing and Surface Scattering and Emission Theory*; Addison-Wesley: London, UK, 1982; p. 1064.



24. Labun, J.; Soták, M.; Kurdel, P. Technical note innovative technique of using the radar altimeter for prediction of terrain collision threats. *J. Am. Helicopter Soc.* **2012**, *57*, 85–87. [[CrossRef](#)]
25. Kayton, M.; Fried, W.R. *Avionics Navigation Systems*; John Wiley & Sons: New York, NY, USA, 1997; p. 773, ISBN 0-471-54795-6.



© 2018 by the authors. Licensee MDPI, Basel, Switzerland. This article is an open access article distributed under the terms and conditions of the Creative Commons Attribution (CC BY) license (<http://creativecommons.org/licenses/by/4.0/>).